Daytime Image Measurement and Reconstruction for Space Situational Awareness Applications (Paper ID number 4231324)

Michael C. Roggemann, Dennis Douglas, Eric Therkildsen,
David Archambeault, Riki Maeda, David Schultz, Ben Wheeler
Pacific Defense Solutions LLC, Kihei, HI

Abstract

An operational technology for imaging satellites during the daytime hours would vastly increase the ability of optical space situational awareness (SSA) systems to gather information about satellites. During the day the atmospheric seeing is generally worse than in terminator, and the contribution of sky background noise to the image measurement is significant. We have developed a straightforward model for estimating the signal-to-noise ratio of the image during daytime hours, and have used this model to help select the optimal wave band for imaging during daytime hours. In this paper we describe the model, and present results. We also present simulated bispectrum images of a space object imaged in strong background at the wavelength of 800 nm. We find that imaging satellites in the near infrared band of 765-915 nm during daytime conditions will often be feasible.

Introduction

Historically, SSA imaging operations have been conducted in terminator conditions – i.e., when the satellite is illuminated by the sun, but the observatory is not. Expanding the ability to image satellites after the morning terminator and before the evening terminator would vastly increase the number of satellites which could be observed. The key issues for successful daytime imaging are minimizing the effects of background radiation in the detectors for the imaging system and the tracker, and overcoming the effects of atmospheric turbulence, which is expected to be stronger during the day. The primary means of addressing these issues is by making judicious choices of operating bands for the various components of the imaging system, including the tracking and imaging cameras, and accounting for the presence of background radiation in the image processing algorithms. In this paper we discuss the physical effects which dominate wave band allocation: atmospheric transmission windows; the spectral radiance of the sky; spectral transmission of the optics, and the quantum efficiency and noise parameters of the detectors available. We have developed a relatively simple image domain signal-to-noise ratio (SNR)-based metric we call the pixel SNR (PSNR) to perform a preliminary assessment of these tradeoffs. The PSNR metric is described in this paper, and representative results are presented. Due to the strong spectral dependence of atmospheric transmission windows, sky background radiance, transmittance of the optical system, and quantum efficiency of the potential detectors, the analysis must of necessity include an accounting for these effects. We have also developed a simulation of imaging under conditions of high background using the bispectrum technique [Roggemann, 1996], and present some representative results here. To obtain quantitative results we use as an example the Advance Electro-Optical System (AEOS) telescope located atop Mt. Haleakala, on the island of Maui, Hawaii.

The key result of this paper is that the PSNR metric indicates that operation in the near infrared band of 765-915 nm is optimal primarily because the sky background is relatively low in this band compared to visible bands during the day, low read noise, high quantum efficiency detectors exist in this band, targets illuminated by the sun are relatively bright, and atmospheric transmission windows exist in this band. In addition, atmospheric turbulence effects in this band are weaker than at the shorter wavelengths often used for terminator observations. Image reconstruction using speckle imaging techniques is feasible under high background conditions, though performance degrades, as the sky brightness increases.

Due to the effects of atmospheric turbulence the measured images will also be corrupted by random turbulence-induced blurring effects. Since use of an adaptive optics system is not presently envisioned, it will be necessary to apply post detection image reconstruction using either the speckle imaging technique [Roggemann, 1996], or multi-frame blind deconvolution (MFBD) [Schulz, 1993].

Considerations for optimizing the performance of the post detection image processing may also affect the final choice of operating band, however, this matter is deferred to future publications.

The remainder of this paper is organized as follows. In the next section we present the PSNR metric. In the following section we discuss the inputs to the PSNR model, and present some representative results. A simulation of speckle imaging under high background conditions is then described, and representative results are presented. Conclusions are discussed in the final section.

The PSNR Metric

We seek to optimize the band allocation based on the signal-to-noise ratio (SNR) of the measured photo-electron counts for detectors illuminated by light from the target. We assume that the target is a Lambertian reflecting spherical object in orbit described by two parameters: (1) its brightness, as described by its visual magnitude, adjusted for the spectrum of the sun; and (2) its angular subtense. We do not account for the spectral reflectivity of the satellite in this analysis, though this effect will certainly affect image quality in the reconstructed images. The SNR for a pixel illuminated by the target is

$$SNR = \frac{K_T^{IMG}}{\sqrt{K_T^{IMG} + K_B + K_D + \sigma_{RN}^2}} \tag{1}$$

where K_T is the mean number of photo-electrons generated by the target in a single pixel which is fully illuminated by the average image of the target during the exposure time τ, K_B is the mean number of photo-electrons generated by the background in this pixel during the exposure time, K_D is the mean number of electrons generated by dark current in the detector per exposure time, and σ_{RN} is the RMS number of read noise electrons per pixel per readout in the detector. K_T is calculated using

$$K_T^{IMG} = \int_t^{t+\tau} \int_{\lambda_1}^{\lambda_2} P(\lambda, t)\eta_{ATM}(\lambda)\eta_{OPT}(\lambda)\eta_{QE}(\lambda)\, \mathrm{d}\lambda d\tau \tag{2}$$

where $P(\lambda, t)$ is the number of photons per time that would arrive at the aperture in the absence of the atmopshere as a function of wavelength λ and time t, $\eta_{ATM}(\lambda)$ is the spectral transmittance of the atmosphere, $\eta_{OPT}(\lambda)$ is the spectral transmittance of the optics, $\eta_{QE}(\lambda)$ is the spectral quantum efficiency of the detector, and the interval (λ_1, λ_2) defines the spectral window which falls on the detector. We will assume that over short time scales $P(\lambda, t)$ will not vary in time, so that $P(\lambda, t) \rightarrow P(\lambda)$ and as a result

$$K_T^{IMG} = \tau \int_{\lambda_1}^{\lambda_2} P(\lambda)\eta_{ATM}(\lambda)\eta_{OPT}(\lambda)\eta_{QE}(\lambda)\, \mathrm{d}\lambda \tag{3}$$

It should be noted that K_T^{IMG} represents the total mean number of signal photons per integration time falling on the detector. Computing the mean number of signal photons per pixel per integration time requires a model for the image size, which is presented after a discussion of the contribution of the sky background to the measured image.

The mean number of background counts can be estimated by using the Air Force Research Laboratory (AFRL) Phillips Laboratory Expert-assisted User Software (PLEXUS) code to compute the radiance of the sky for the conditions of interest, and then using standard radiometric techniques to calculate the rate of photo-electron generation in the detector. (A description of PLEXUS is available on-line at: http://www.kirtland.af.mil/library/factsheets/factsheet.asp?id=7917.) Let the spectral radiance of the sky be represented by $L_e^B(\lambda)$ in W/(m^2 · sr · μm). The mean number of counts K_B from the sky background intercepted by a single square detector with angular subtense of each side represented by θ_{DAS} , so that the associated solid angle is $\Omega_{DAS} = \theta_{DAS}^2$, is given by

$$K_B = \frac{\tau A_R \Omega_{DAS}}{\left(hc/\lambda\right)} \int_{\lambda_1}^{\lambda_2} L_e^B(\lambda)\, \eta_{ATM}(\lambda) \eta_{OPT}(\lambda) \eta_{QE}(\lambda)\, \mathrm{d}\lambda \tag{4}$$

where A_R is the area of the receiving aperture, h is Planck's constant, c is the speed of light in a vacuum, and $\bar{\lambda}$ is the mean wavelength. Since the post detection image reconstruction algorithms are optimal for Nyquist sampled data we shall set $\theta_{DAS} = \lambda/(2D)$, where D is the aperture diameter.

$P(\lambda)$ is computed using a standard code which assumes the target is a spherical Lambertian reflector illuminated by the sun at a distance equal to the mean distance of the earth from the sun. Dark current is generated at a temperature-dependent constant rate in the detector which is generally given in the specification sheets provided by the manufacturer. The RMS read noise is function of the design of the readout and preamplification electronics of a camera, and is also generally given in the specification sheets provided by the manufacturer. The required integrations to evaluate K_T and K_B are performed using a numerical boxcar integration over PLEXUS outputs.

To compute the SNR per pixel illuminated by the target it is necessary to implement a target and associated image model. In the present case we assume the target is a uniformly illuminated disk specified by its visual magnitude, and angular subtense θ_{TGT}. The average image of this target has diameter in the image plane of approximately $\theta_{IMG} = \theta_{TGT} + \lambda/r_0 + \lambda/D$, where r_0 is the Fried parameter characterizing the strength of the turbulence. The solid angle subtended by the image is $\Omega_{IMG} = \pi\left(\frac{\theta_{IMG}}{2}\right)^2$, and hence the number of pixels illuminated by the average target pixel is estimated by $N_{TGT} \approx \Omega_{IMG}/\Omega_{DAS}$. The mean number signal photo-electrons per pixel per integration time for a pixel illuminated by the target can now be estimated from

$$K_T = \frac{K_T^{IMG}}{N_{TGT}} \tag{5}$$

As an example, the average image associated with a disk target subtending 30 μRad sampled at the Nyquist angular sampling rate and imaged through turbulence characterized by r_0=10 cm at 500 nm, imaged by the 3.63 m diameter AEOS telescope at the mean wavelength of 1.1 μm would occupy approximately 40,895 pixels in the image plane.

Turbulence is modeled in this SNR per pixel calculation by specifying the Fried parameter at the wavelength of 500 nm and scaling this value to the appropriate mean wavelength. The scaling law is

$$r_0(\bar{\lambda}) = r_0(500\ nm)\left(\frac{\bar{\lambda}}{500\ nm}\right)^{6/5} \tag{6}$$

Optical System Model Inputs

As described in the section above, the PSNR model requires a number of physical inputs: sky radiance, atmospheric transmission, detector quantum efficiency, brightness of the target, transmission of the optical system, aperture area, and r_0. We now provide representative examples of these inputs. Sky radiance and atmospheric transmission data was obtained using PLEXUS. Look angles were taken from 0-340 degrees in 20-degrees steps in azimuth and 5-90 degrees in 5-degree steps in elevation. It should be noted that PLEXUS sky radiance data does not take into account specular solar effects, such that if one were to "point" the receiver at the sun only the corresponding non-specular sky background is calculated. Data samples looked from 5 AM to noon HST in 1 hour steps on June 21, 2010 (the summer solstice). The sky background and transmission were averaged over each time sample over all look angles. This yields a macroscopic scenario insensitive to solar phase angle that concentrates on all look angles for a given time of day. The wavelength range was set from 500 nm to 2500 nm in 1 nm steps. MODTRAN 4.0 V2R1 was used within PLEXUS as the atmospheric modeling code. Sky radiance results are presented in Figure 1. Sunrise occurs at 5:45

AM Hawaii Time on the summer solstice. The night/terminator and daylight cases are plotted separately to shorten the y-axis range in the semi-log plots in Figure 1. During daylight hours the sky radiance increases as a function of daylight hour and decreases at longer wavelengths. The latter effect is shown by the slope of the radiance curves over the wavelength range during the day.

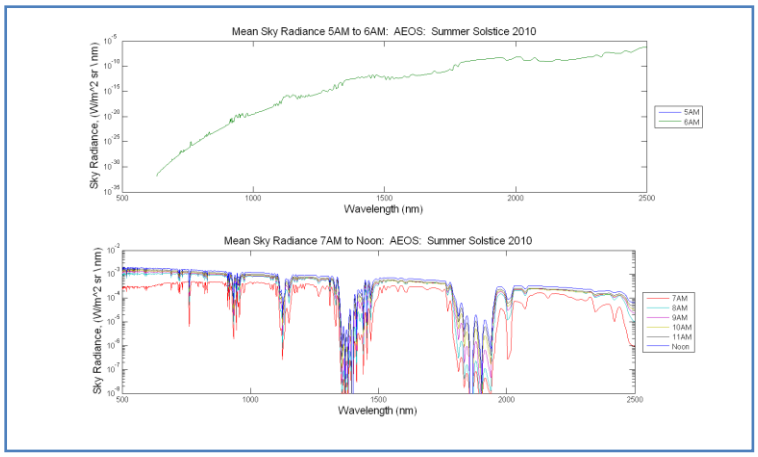

Figure 1. PLEXUS calculated sky radiance. Averaged over time of day and plotted versus wavelength.

PLEXUS also provides atmospheric transmission estimates. Atmospheric transmission was averaged over all look angles for a given time of day. This approach is conservative in that it factors in very low elevation look angles that may not be realizable using conventional imaging techniques. In general, the atmospheric transmission is insensitive to time of day and azimuth look angles. Elevation angle is the outstanding factor in the atmospheric transmission values. Figure 2 illustrates the effects of elevation angle on the atmospheric transmission. It should be noted elevation angle cases smaller than 15 degrees rapidly fall off in transmission due to the exponentially increasing air mass.

Readily available COTS sensor technology was explored to represent the trade space over the 500 nm to 2500 nm wavelength range. The Andor EMCCD Si sensor was chosen to represent the "visible" wavelength range, and is a sensor that the site has access to and is already familiar with through previous projects. It should be noted that the term "visible" is used loosely here to describe the range of wavelengths accessible with a silicon detector, which includes wavelengths well outside those which can be experienced directly by human vision. FLIR Systems sensors were chosen to represent the NIR and SWIR regions. FLIR Systems initially was chosen based on previous sensor trade studies from other programs indicating that the FLIR sensors possessed a lower read noise than other vendors. A future sensor trade study will assemble current sensor parameters from other vendors to ensure that appropriate sensor selection(s) are made. QE data was obtained from Andor and FLIR. The Andor QE data is from the vendor specification sheet, and the FLIR data is measured data obtained from FLIR. Figure 3 illustrates the sensor QEs over the 500 nm to 2500 nm wavelength range. The pixel pitch, array size, read noise and dark current parameters for each sensor were obtained from the vendor's specification sheets, and are presented in Table 1. It should be noted that the read noise and dark current for non Silicon based sensors can vary according to sensor. It is highly recommended that the final sensor(s) be characterized according to QE, read noise, dark current, uniformity, linearity, and diffusion mapping. This sensor characterization would be carried out in a suitable laboratory.

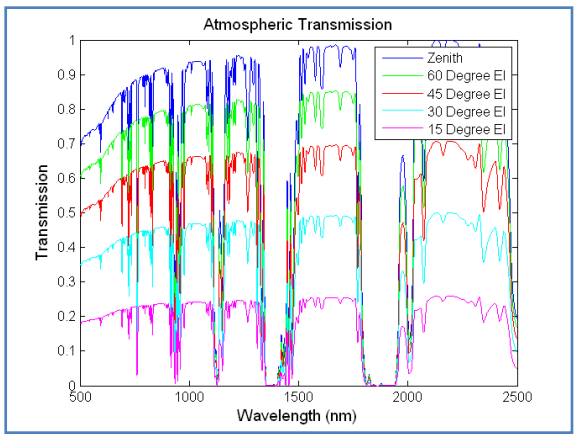

Figure 2. PLEXUS calculated atmospheric transmission versus wavelength and elevation look angle.

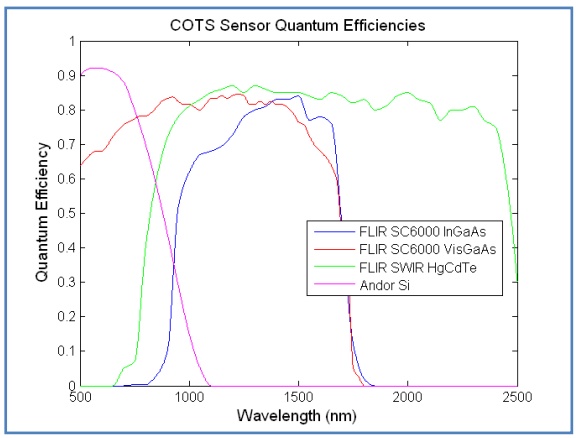

Figure 3. Sensor QEs used in single pixel SNR model.

Table 1. Key parameters of the five cameras researched in this study. N_X = number of detectors in horizontal dimension, N_Y = number of detectors in the vertical dimension. The symbol e- represents electrons.

Camera Name	Pixel Pitch (μm)	(N_X, N_Y)	σ_{RN} (e-)	K_D [e-/(pixel · sec)]	Well Depth (e-)
FLIR SC6000 InGaAs	25	(640,512)	70	6.4×10^4	3.5×10^6
FLIR SC6000 VisGaAs	25	(640,512)	70	6.4×10^4	3.5×10^6
FLIR SWIR HgCdTe	30	(320,256)	250	6.4×10^4	1.3×10^6
Andor EMCCD Si	8	(1004,1002)	< 1	0.17	30,000

The optical transmission of the AEOS system was used to present representative results for this paper. AEOS has a complicated beam train which includes the option of using the adaptive optics system, or bypassing it for better transmission efficiency in the absence of adaptive optics compensation of the beam. The AEOS transmission data was obtained detailing the transmission curves for the AEOS AO dichroic and 50/50 beam splitters in the optical path. Theoretical reflectivity data was used for each mirrored optical interface based on the mirror coating type, and the transmission curve was factored in for the Infrasil Coude window. The theoretical transmission

curve was scaled to a zero point measurement in the I-band performed by Dr. Doyle Hall in late 2004 [Hall, 2004]. Dr. Hall's zero point measurement calculated that at 790 nm the net throughput of the reflective optics to the VisIm path is between 25% and 35%. The transmission scaling was performed by adjusting the theoretical transmission roll-up for all optical elements uniformly over the 500 nm to 2500 nm wavelength range such that the final curve matched Dr. Hall's measurements at 790 nm. Figure 4 shows the overall optical transmission through AEOS telescope.

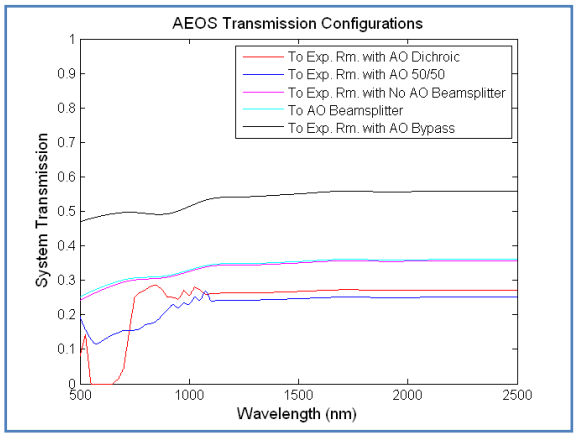

Figure 4. The AEOS optical transmission for multiple configurations.

PSNR Results

The PSNR was derived over the 500 nm to 2500 nm range by implementing 1 nm width spectral bands in the model over the complete wavelength range. This approach would unlikely be implemented in a physical imaging system, yet yields much insight into the set of optimized wavelength wavebands through which a physical system would incorporate. The following series of plots show the PSNR cases as a function of 1 nm width spectral filtering for the various AEOS optical path configurations. Representative results are presented in Figs. 5, 6, and 7. Inputs used in computing these figures are provided in Tables 1 through 4. We now discuss the results.

Figure 5 shows the PSNR for 1 nm wavelength bins as a function of wavelength for the cameras studies here, for different times of day. Figure 5 was computed using the input parameters are provided in Tables 1 and 2. Inspection of Fig. 5 shows that the EMCCD sensor has a clear advantage in PSNR over all other sensors studied. The read noise term dominates the non EMCCD sensors and limits single pixel SNR variation as a function of time of day. The read noise term dominates the non EMCCD sensors and limits the PSNR variation as a function of time of day.

Table 2. Input parameters for Figure 5.

Parameter	Value
Object Visual Magnitude	Mv = 2
Integration Time	5 ms
Object Angular Extent	10 µrad
r_0	10 cm @ 500nm
Nyquist Sampling	1X
Optical Path	AEOS AO Bench Bypass to Exp. Rm.

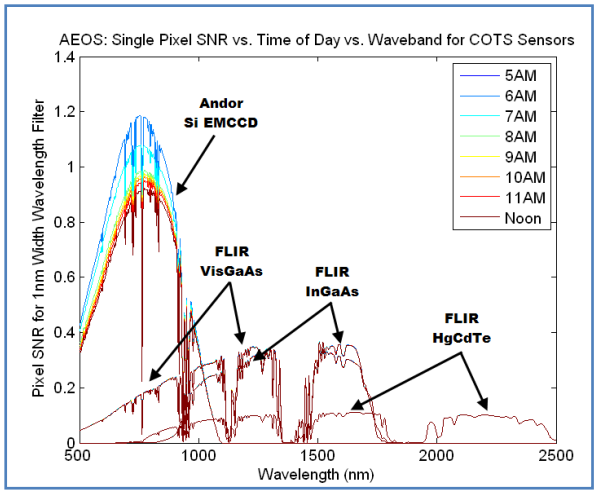

Figure 5. PSNR for 1 nm wavelength bins as a function of wavelength for the cameras studies here, for different times of day. Input parameters are provided in Tables 1 and 2.

The following multi variable set of plots explore the single pixel input parameters in more detail. All multi variable cases use the AEOS system path through to AO bench but with no AO beam splitter in place. Other optical paths can be easily examined. The visual magnitudes and r_0 values used provide insight into the effects of input parameter variation. Some of these results are presented in Figs. 6, 7, and 8, with the inputs described in Tables 3, 4, and 5, respectively. The camera choice in each wave band is implicit based on the pass band of the camera. Figure 6 shows the PSNR as a function of wavelength for three visual magnitudes, Fig. 7 shows the PSNR as a function of wavelength for three values of the object angular extent, and Fig. 8 shows the PSNR as a function of wavelength for three values of r_0.

Table 3. Input parameters for Figure 6.

Parameter	Value
Object Visual Magnitude	Mv Varied from Mv=1 to Mv=3
Integration Time	5 ms
Object Angular Extent	10 µrad
r_0	10 cm @ 500nm
Nyquist Sampling	1X
Optical Path	Through AEOS AO Bench with AO beam splitter bypassed to Exp. Rm.

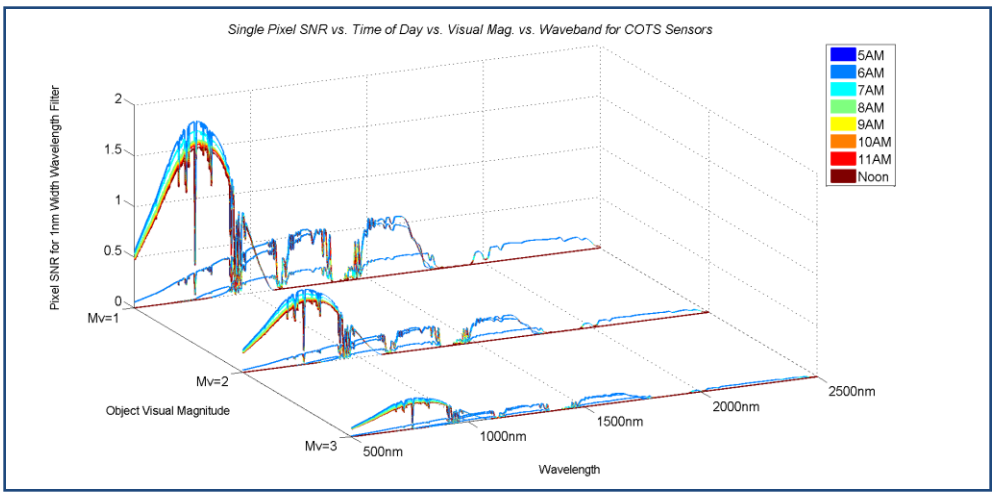

Figure 6. Single pixel SNR with object visual magnitude varied.

Table 4. Input parameters for Figure 7.

Parameter	Value
Object Visual Magnitude	Mv = 2
Integration Time	5 ms
Object Angular Extent	Varied from 10 µrad to 30 µrad
r_0	10 cm @ 500nm
Nyquist Sampling	1X
Optical Path	Through AEOS AO Bench with AO beam splitter bypassed to Exp. Rm.

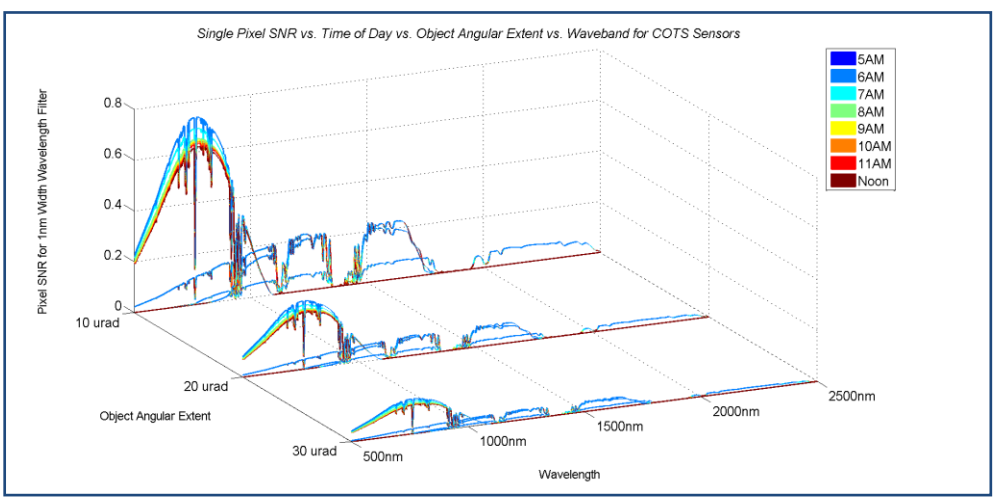

Figure 7. Single pixel SNR with object angular extent varied.

Table 5. Input parameters for Figure 8.

Parameter	Value
Object Visual Magnitude	Mv = 2
Integration Time	5 ms
Object Angular Extent	10 µrad
r_0	Varied from 3 cm to 9 cm @ 500nm
Nyquist Sampling	1X
Optical Path	Through AEOS AO Bench with AO beam splitter bypassed to Exp. Rm.

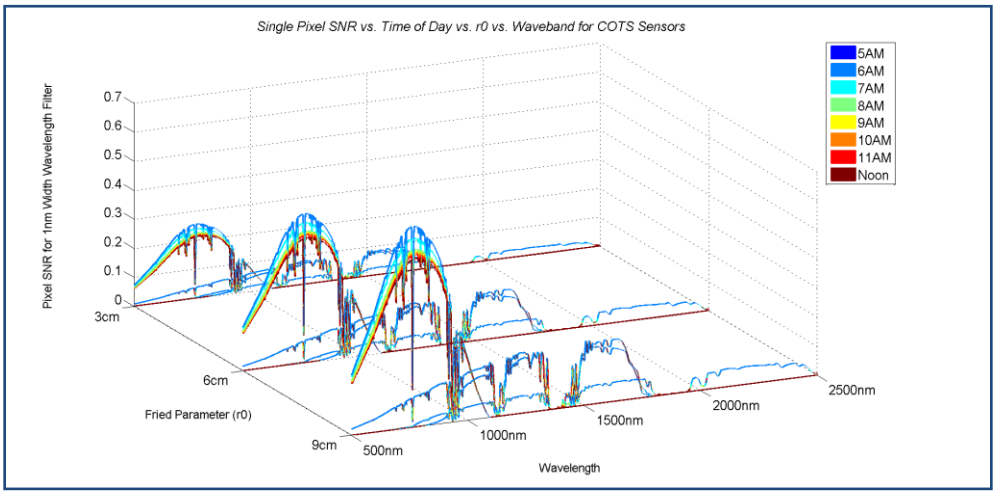

Figure 8. Single pixel SNR with r0 varied.

Inspection of Fig. 6 shows that increasing the visual magnitude yields a significant PSNR decrease, as expected. We would expect that the PSNR would generally decrease for orbiting solar illuminated objects as the object angular extent got smaller. However, in this model, the visual magnitude is fixed regardless of the object's angular extent. However, inspection of Fig. 7 shows that the PSNR increases for objects with a smaller angular extent, since there are fewer overall pixels illuminated by the object. This behavior is an artifact of the relatively simple approach taken here of specifying the object angular extent and visual magnitude independently, and can be easily remedied by using a more realistic radiometric model for the object as a function of angular extent. Inspection of Fig. 8 shows the expected result that decreasing r_0 results in spreading the light on the focal plane array.

The 1 nm filtering single pixel SNR analysis yields insight into the appropriate overall waveband selections. The previous plots indicate that regardless of input parameters the atmospheric transmission dictates where the cut-off points are for single pixel SNR. Figure 9 illustrates these SNR cut-off points in wavelengths, with color coding to show the optimal waveband as a function of time of day. For the hours immediately after morning terminator the band of 765-915 nm yields the highest PSNR and would by this metric be the optimal band for imaging in this time frame.

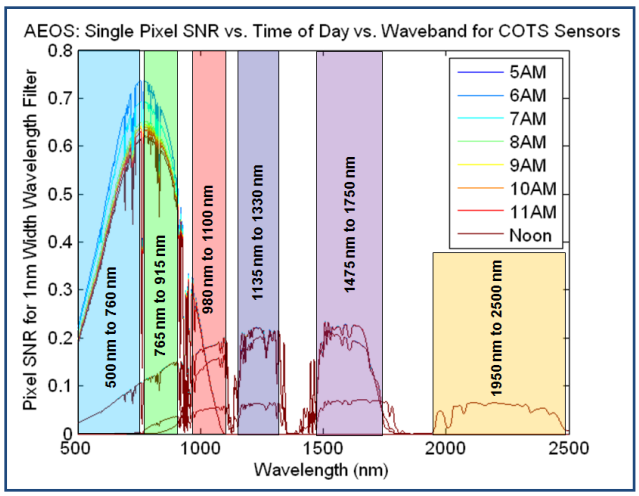

Figure 9. Single pixel SNR cut-off points as a function of wavelength.

<u>Simulation of Imaging in High Background Conditions</u>

A simulation of speckle imaging measurement and post detection processing using a speckle imaging technique was developed to study the effects of high background levels on the subjective quality of the reconstructed images. In this section we briefly describe this model, and present some representative results.

The simulation is based on the standard Fourier optics model of image formation [Goodman, 2005]. A time-varying aberration in the pupil of the telescope is modeled by placing a single random phase screen with user-specified Fried parameter r_0 in the pupil of the telescope, and calculating the associated optical transfer function (OTF). The instantaneous OTF is multiplied by the Fourier transform of the object, and this product is inverse Fourier transformed to obtain a noise free version of the image associated with the current realization of the atmospheric turbulence. The noise free image is normalized so that the sum of the intensities equals a user-specified mean photo-electron arrival rate due to the target $\overline{K}_{Tgt}$. The background is modeled as uniform, and the background mean photo-electron arrival rate is specified in counts per pixel per frame $\overline{K}_{Bk}^{pix}$. The images containing the mean count rate due to the target and the mean count rate due to the background are summed, so that the total mean count rate is $\left(\overline{K}_{Tgt} + P\overline{K}_{Bk}^{pix}\right)$, where P is the total number of pixels in the image, and the result is passed through a Poisson random number generator. The AEOS aperture, which as primary diameter of 3.63 m, and obscuration diameter of 0.18 m was modeled for imaging at 800 nm wavelength. Both the object and the image were Nyquist sampled in 300 × 300 sample arrays. The object is show in Fig. 10. Reference star images were also computed for the purpose of calibrating the power spectral density (PSD) of the measured images of the object for the combined effects of diffraction due to the finite size of the telescope, and atmospheric turbulence effects. Hence, with a fixed object the images can be specified by the three parameters: $\overline{K}_{Tgt}$, $\overline{K}_{Bk}^{pix}$, and r_0.

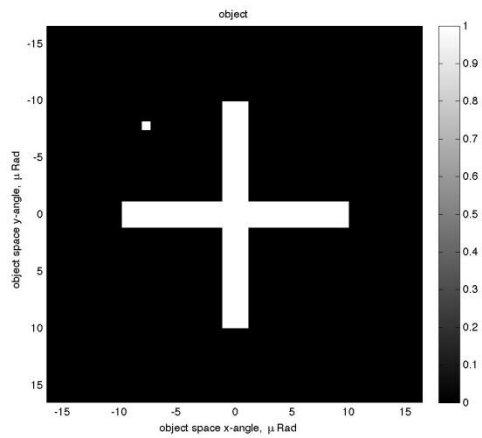

Figure 10. Object used in imaging simulations.

When background is present it is necessary to pre-process the measured images before implementing speckle image post processing due to the fact that the zero frequency component in the Fourier transform of the measured images is strongly affected by the background radiation. The pre-processing approach taken here is to estimated the background level of the measured images by computing the mean of a 20 × 20 pixel subregion in each corner of the images and subtracting this estimate of the mean from every pixel in every measured image. The resulting pixel values in the regions not containing illumination from the target is then zero mean, and approximately Gaussian at the high count rates of interest here [Snyder, 1991]. The standard deviation of this background process is computed for the 20 × 20 pixel subregions after mean removal, and used as read noise bias term in both the bispectrum and PSD bias removal steps [Roggemann, 1996]. The mean removed images can be summed to estimate the number of photo-electrons per image to use in the bias removal for the PSD and bispectrum. Data sets of 200 images created with independent phase screens were processed to estimate the simulated images.

The resulting images were processed with a bispectrum processing algorithm for the fixed values of $\overline{K}_{Tgt} = 5 \times 10^6$, $r_0 = 0.14$ m at wavelength of 800 nm, and increasing values of $\overline{K}_{Bk}^{pix}$ to demonstrate the effects of increasing background on the reconstructed images. Results are shown in Fig. 11 for the cases: (a) $\overline{K}_{Bk}^{pix}$ = 500 per pixel per frame; (b) $\overline{K}_{Bk}^{pix}$ =2,000 per pixel per frame; (c) $\overline{K}_{Bk}^{pix}$ =8,000 per pixel per frame; (d) $\overline{K}_{Bk}^{pix}$ =12,000 per pixel per frame; (e) $\overline{K}_{Bk}^{pix}$ =25,000 per pixel per frame; and (f) $\overline{K}_{Bk}^{pix}$ =50,000 per pixel per frame. Inspection of Fig. 11 shows an example of how performance degrades with increasing background levels. Even at the high background count rates in Figs. 11 (e) and (f) the main features of the object can be discerned, though it is anticipated that small details may be unreliably imaged due to noise effects.

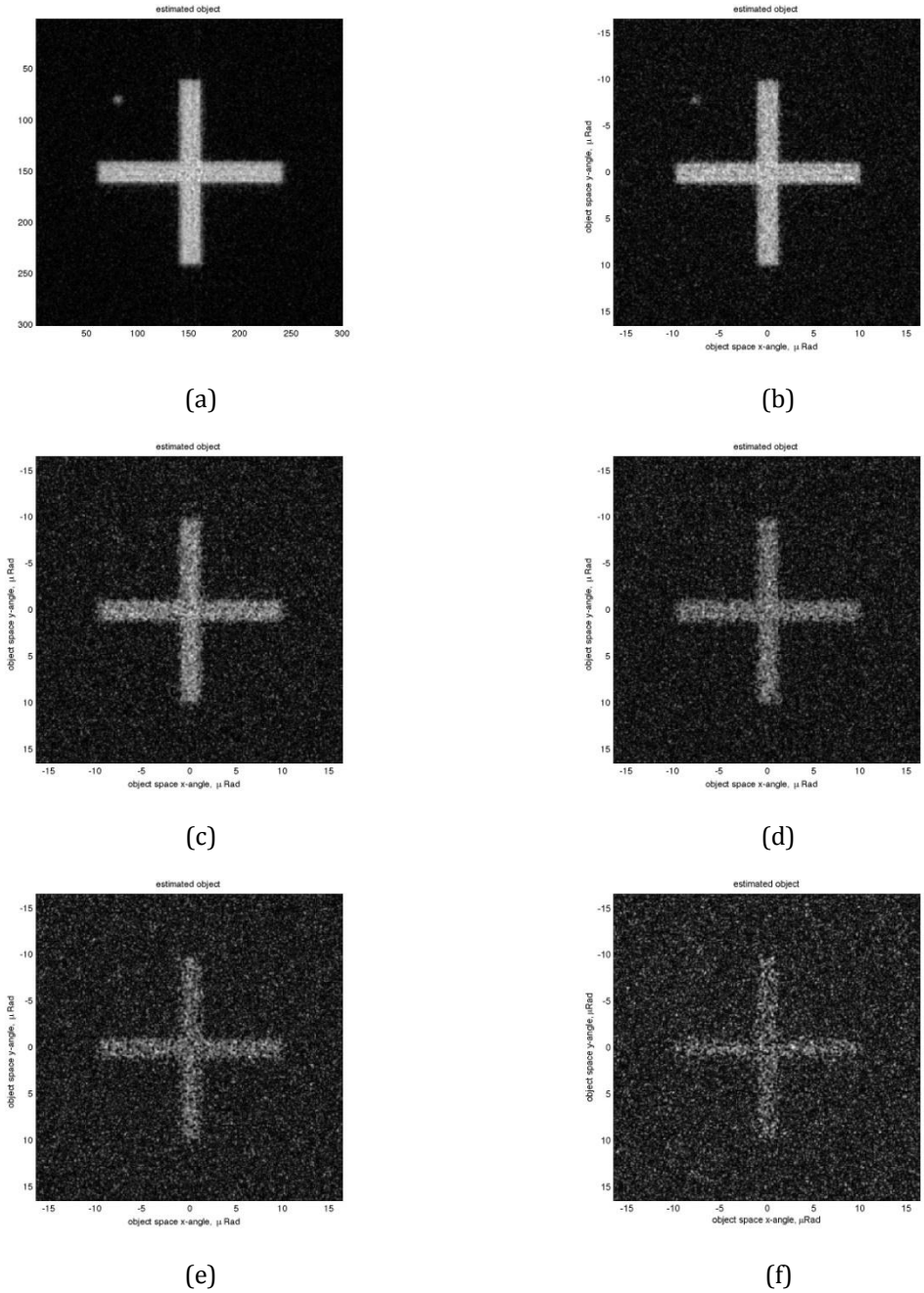

Figure 11. Example reconstructed images for the input parameters described above, with background counts $\overline{K}_{Bk}^{pix}$ given by: (a) $\overline{K}_{Bk}^{pix}$=500 per pixel per frame; (b) $\overline{K}_{Bk}^{pix}$=2,000 per pixel per frame; (c) $\overline{K}_{Bk}^{pix}$=8,000 per pixel per frame; (d) $\overline{K}_{Bk}^{pix}$=12,000 per pixel per frame; (e) $\overline{K}_{Bk}^{pix}$=25,000 per pixel per frame; and (f) $\overline{K}_{Bk}^{pix}$=50,000 per pixel per frame.

Conclusion

The PSNR results presented here show a significant SNR advantage in the Silicon sensor range over the set of 1 nm filters across the 500 nm to 915 nm wavelength range. This is mainly a factor of the low read noise using the Andor EMCCD sensor, as the sensor read noise dominates the SNR. This is evident in the overlapping PSNRs with respect to time of day for the NIR/SWIR sensors that contain much higher read noise values than the Andor EMCCD sensor. The sensor read noise supersedes all other factors including sky background in the look angle averaged SNR single pixel analysis. The high dark current values for the NIR/SWIR sensors contribute very little to the noise in these cases, and are greatly mitigated by the short exposures required in speckle imaging. The high PSNR in the Silicon range is very encouraging since it is desired to image at shorter wavelengths for greater resolution. We also created some examples of reconstructed images in the presence of high background levels. Performance clearly degrades as the background level rises, but some details of the image can be discerned even at very strong background levels.

References

[Goodman, 2005] J. W. Goodman, *Introduction to Fourier Optics, Third Edition*, Roberts & Company Publishers, Greenwood Village, CO, 2005.

[Hall, 2004] *Estimated AEOS Telescope Throughput at 790nm*. Dr. Doyle T. Hall, The Boeing Co., 2004.

[Roggemann, 1996] M. C. Roggemann, and B. M. Welsh, *Imaging Through Turbulence*, CRC Press, Boca Raton, FL, 1996.

[Schulz, 1993] Timothy J. Schulz, "Multiframe blind deconvolution of astronomical images", *J. Opt. Soc. Am. A*, vol. 10, p1064-1073, 1993.

[Snyder, 1991] D. L. Snyder, and M. I. Miller, *Random Point Processes in Time and Spac,* Springer-Verlag, 1991.